A&A 634, A55 (2020)
https://doi.org/10.1051/0004-6361/201936104

Astronomy & Astrophysics

Observational constraints on the origin of the elements

II. 3D non-LTE formation of Ba II lines in the solar atmosphere

A. J. Gallagher[1], M. Bergemann[1], R. Collet[2], B. Plez[3], J. Leenaarts[4], M. Carlsson[5,6], S. A. Yakovleva[7], and A. K. Belyaev[7]

[1] Max-Planck-Institut für Astronomie, Königstuhl 17, 69117 Heidelberg, Germany
e-mail: gallagher@mpia-hd.mpg.de
[2] Department of Physics and Astronomy, Aarhus University, Ny Munkegade 120, 8000 Aarhus, Denmark
[3] LUPM, UMR 5299, Université de Montpellier, CNRS, 34095 Montpellier, France
[4] Institute for Solar Physics, Department of Astronomy, Stockholm University, AlbaNova University Centre, 106 91 Stockholm, Sweden
[5] Rosseland Centre for Solar Physics, University of Oslo, PO Box 1029 Blindern, 0315 Oslo, Norway
[6] Institute of Theoretical Astrophysics, University of Oslo, PO Box 1029 Blindern, 0315 Oslo, Norway
[7] Department of Theoretical Physics and Astronomy, Herzen University, St Petersburg 191186, Russia

Received 14 June 2019 / Accepted 1 October 2019

ABSTRACT

Context. The pursuit of more realistic spectroscopic modelling and consistent abundances has led us to begin a new series of papers designed to improve current solar and stellar abundances of various atomic species. To achieve this, we have begun updating the three-dimensional (3D) non-local thermodynamic equilibrium (non-LTE) radiative transfer code, MULTI3D, and the equivalent one-dimensional (1D) non-LTE radiative transfer code, MULTI 2.3.
Aims. We examine our improvements to these codes by redetermining the solar barium abundance. Barium was chosen for this test as it is an important diagnostic element of the *s*-process in the context of galactic chemical evolution. New Ba II + H collisional data for excitation and charge exchange reactions computed from first principles had recently become available and were included in the model atom. The atom also includes the effects of isotopic line shifts and hyperfine splitting.
Methods. A grid of 1D LTE barium lines were constructed with MULTI 2.3 and fit to the four Ba II lines available to us in the optical region of the solar spectrum. Abundance corrections were then determined in 1D non-LTE, 3D LTE, and 3D non-LTE. A new 3D non-LTE solar barium abundance was computed from these corrections.
Results. We present for the first time the full 3D non-LTE barium abundance of $A(\mathrm{Ba}) = 2.27 \pm 0.02 \pm 0.01$, which was derived from four individual fully consistent barium lines. Errors here represent the systematic and random errors, respectively.

Key words. hydrodynamics – radiative transfer – line: formation

1. Introduction

Barium is a key element that is used in heavy element studies in stars. Its abundance patterns in the halo, in field stars, and in clusters have been carefully measured over the past several decades. Barium, like most other heavy elements, mostly forms through a series of neutron captures through either the rapid (*r*-) process or slow (*s*-) process channels. These two neutron capture channels have very different sites. After the discovery and analysis of 2017gfo (the electromagnetic counterpart of GW170817 Valenti et al. 2017), it is highly probable that the *r*-process mostly occurs in neutron star mergers (Thielemann et al. 2011). Conversely, the majority of barium in the Sun (81% Arlandini et al. 1999) ostensibly formed through the *s*-process in thermally pulsing asymptotic giant branch (TP-AGB) stars (Smith & Lambert 1988). However, other sites for the *s*-process and *r*-process most likely exist. The barium isotope ratio, f_{odd}[1], of a star is a useful quantity as it provides precise information on the *s*- and *r*-process contribution, but it is exceedingly difficult to measure. Therefore, this information is only measured in some thick-disk and halo stars, where this parameter is most interesting (Magain & Zhao 1993; Magain 1995; Mashonkina et al. 1999; Gallagher et al. 2010, 2012, 2015).

Most abundances, except for those such as lithium, whose abundance is measured in absolute units, are measured relative to the solar abundances. This helps to mitigate systematic errors within spectroscopic abundances and yields additional information about stellar populations, evolutionary stages, and ages that measurements in absolute units might not. As a result, the solar abundances are extremely important to stellar astrophysics. Consequently, very accurate measurements of the solar abundance are needed that employ sophisticated model atmospheres and spectrum synthesis techniques such as three-dimensional (3D) hydrodynamics and non-local thermodynamic equilibrium (non-LTE) physics. In recent years, with the development of faster and larger computers, it has been possible to develop and implement these methods (Asplund et al. 2003; Steffen et al. 2015; Klevas et al. 2016; Amarsi et al. 2016; Mott et al. 2017; Amarsi & Asplund 2017; Nordlander et al. 2017).

One of the main aims of this series of papers is to report on our development of the one-dimensional (1D) and 3D statistical equilibrium codes MULTI 2.3 (Carlsson 1986) and MULTI3D

[1] $f_{\mathrm{odd}} \equiv \left[N(^{135}\mathrm{Ba}) + N(^{137}\mathrm{Ba})\right]/N(\mathrm{Ba})$.

(Leenaarts & Carlsson 2009) as we include new or better physics into their program flows. Given how important barium is to galactic chemical evolution studies because it traces the effect of neutron-capture nucleosynthesis, we present a thorough analysis of the solar barium abundance using a handful of Ba II optical lines that are computed using the two statistical equilibrium codes and the same barium model atom.

The statistical equilibrium of Ba II has previously been a subject of several detailed studies (Mashonkina & Bikmaev 1996; Mashonkina et al. 1999; Shchukina et al. 2009; Andrievsky et al. 2009; Korotin et al. 2015). The first such study was conducted by Gigas (1988) in Vega. There are, however, important differences between our work and these earlier studies. First, we use the new quantum-mechanical rates for transitions caused by inelastic collisions with hydrogen atoms from Belyaev & Yakovleva (2018). We also examine the effect that dynamical gas flows have on Ba II by utilising a 3D radiative hydrodynamical model to compute full 3D non-LTE radiative transfer, as well as 3D LTE, 1D LTE, and 1D non-LTE. Ab initio collisional damping from Barklem et al. (2000) was included in the linelist.

It has been observationally confirmed that the Ba II resonance line at 4554 Å is sensitive to the chromospheric effects[2], and a polarised spectrum of the resonance line is therefore also sensitive to the quantum interferences (see, e.g. Kostik et al. 2009; Shchukina et al. 2009; Belluzzi & Trujillo Bueno 2013; Smitha et al. 2013; Kobanov et al. 2016). This is beyond the scope of this paper, however.

The paper is structured as follows. In Sect. 2 we describe the observations, we detail the model atmospheres, model atoms, and spectral synthesis codes; in Sect. 3.2 we discuss the effect that various model assumptions have on our results; in Sect. 5 we describe the analysis and results from our Ba II line analysis; and in Sect. 6 we summarise the study.

2. Models and observations

2.1. Solar spectrum

The solar spectrum was taken from the Kitt Peak National Observatory (KPNO) solar atlas published by Kurucz et al. (1984). This solar atlas covers the spectral range of 3000–13 000 Å at a typical resolution $R \equiv \frac{\lambda}{\Delta\lambda} = 400\,000$. Although newer solar spectra exist, such as the PEPSI spectrum provided by Strassmeier et al. (2018), we chose to work with the former atlas because it has a very high resolution, roughly twice that of the latter. Nevertheless, comparisons of these two spectra have previously been made and they were found to be in very good agreement with one another (Osorio et al. 2019).

2.2. 1D model atmosphere

We used the MARCS model atmosphere that was computed for the Sun from the opacity-sampled grid published in Gustafsson et al. (2008). The solar parameters of this model are $T_{\rm eff}/\log g/[{\rm Fe/H}] = 5777/4.44/0.00$ and include a mixing length parameter, $\alpha_{\rm MLT} = 1.50$. The solar composition used to compute the model opacities is based on those published in Grevesse et al. (2007).

2.3. 3D model atmosphere

We used the solar STAGGER (Nordlund et al. 1994; Nordlund & Galsgaard 1995) model with stellar parameters

[2] Both FAL-C semi-empirical models and a 3D radiative hydrodynamical model from Asplund et al. (2000) were used.

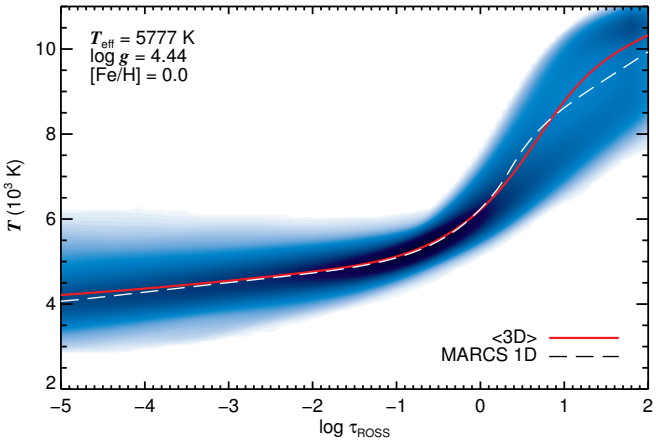

Fig. 1. Temperature structure in 3D, 1D, and ⟨3D⟩.

$T_{\rm eff}/\log g/[{\rm Fe/H}] = 5777\,{\rm K}/4.44/0.0$ from the STAGGER model atmosphere grid (Collet et al. 2011; Magic et al. 2013). A 3D model consists of a series of computational boxes that represent a time series, which are commonly referred to a snapshots. These snapshots are selected from a larger time series of snapshots that are produced from the STAGGER code and are selected at a time when the simulation has reached dynamical and thermal relaxation. For our purposes and for the sake of time, we chose to work with five snapshots, each consisting of 240 × 240 × 230 grid points that cover a geometrical volume of 7.96 × 7.96 × 3.65 Mm in the x, y, and z dimensions, respectively. These were used as independent input for our statistical equilibrium code MULTI3D (Sect. 2.5) and then the output was averaged together by applying the ergodic approximation that averaging in time is equivalent to averaging over space. In this case, it is assumed that averaging in time is equivalent to averaging across the solar disk. The emergent fluxes from these snapshots have an equivalent width variance of only ∼0.75 mÅ, suggesting that including further snapshots in the study will not greatly improve the results we present and only increase the computational time.

Line opacities were collected from the MARCS database and were sorted into 12 opacity bins. Continuous absorption and scattering coefficients were taken from Hayek et al. (2010). Importantly, and unlike an equivalent 1D model, 3D models provide x, y, and z velocity fields for every voxel, meaning that post-processing spectrum synthesis codes provide more accurate approximations for the Doppler broadening, including asymmetric line profiles, which result from these gas flows.

We also used the averaged 3D model to help make qualitative comparisons between the full 3D and 1D models, but we did not use it with MULTI 2.3 or MULTI3D. A ⟨3D⟩ model is computed from a 3D model by spatially averaging the thermal structure of the 3D computational box over surfaces of equal Rosseland optical depth. As this can be performed in several different ways, comparing results from different studies that do not specify their averaging techniques is ultimately self-defeating.

Figure 1 depicts the 3D solar temperature structure (blue 2D histogram), along with the 1D MARCS (dashed line) and ⟨3D⟩ (solid red line) temperature structures. It is clear that the average temperature of the full 3D model and the 1D model are fairly consistent in the outermost regions of the atmosphere (as seen by comparing the 1D with the ⟨3D⟩ model). However, in deeper regions of the models, where the continuum usually forms ($\log \tau_{\rm ROSS} \approx 0$), the models begin to diverge. This is mostly due to the differences between the convection that is indicative of the 3D hydrodynamic model atmosphere (which

the ⟨3D⟩ model traces) and the treatment of convection theory (in this case, the mixing length theory) in the 1D model atmosphere.

2.4. MULTI 2.3

MULTI solves the equations of radiative transfer and statistical equilibrium in 1D geometry with 1D model atmospheres. The latest release of MULTI is MULTI 2.3. However, we have made several minor changes to MULTI 2.3 for our purposes, including the ability to compute the detailed balance for charge transfer processes between ions and hydrogen. We include a fixed microturbulence value of 1 km s^{-1} in our computations with the solar MARCS model. The flux data were computed using five μ angles, assuming a Gaussian quadrature scheme taken from Lowan et al. (1942).

2.5. MULTI3D

MULTI3D is an message passing interface (MPI) parallelised, domain-decomposed 3D non-LTE radiative transfer code that solves the equations of radiative transfer using the multi-level accelerated lambda iteration (ALI) method (Rybicki & Hummer 1991, 1992) for 3D model atmospheres. Every element that is modelled by MULTI3D is assumed to have no effect on the model atmosphere, as it is in MULTI 2.3. This is a good assumption for barium because it is not an electron donor, nor does it have a high impact on the overall opacity, unlike magnesium or iron, for example.

At present, it will accept three types of 3D model atmospheres formats as direct input, including those computed using Bifrost (Gudiksen et al. 2011), and STAGGER. While Bifrost models are read using MPI IO, the STAGGER models are, at present, not read this way due to complications in converting byte ordering. However, the added delay to the code run time is minimal and only becomes noticeable when MULTI3D is run on several hundred CPUs. In addition to these two types of model atmospheres, the code will also accept any 3D model formatted so that the temperature, T, density, ρ, electron number density, n_e, and x, y, and z velocity fields are supplied on a Cartesian grid that is both horizontally periodic and equidistantly spaced. Therefore, it is relatively straightforward to convert almost any 3D model into this input format for MULTI3D.

We have introduced new coding for computing fluxes inside MULTI3D along with the appropriate post-processing routines designed to extract the flux data. All of the output flux data computed for the work presented here were calculated using a Lobatto quadrature scheme and the appropriate corresponding weights (Abramowitz & Stegun 1972). At a later stage of this paper series, other quadrature schemes will be introduced, as well as internal routines that will compute fluxes inside MULTI3D and write them as output.

MULTI3D is now capable of accepting model atoms that include hyperfine structure (HFS) and isotope shift information for any atomic transition. This means that lines with highly asymmetric profiles, caused by these effects, can now be adequately modelled by MULTI3D. To test this upgrade, and to test that we could limit the effect of systematic errors dominating the abundances and abundance corrections we provide, we compared 1D spectra computed by both MULTI 2.3 and MULTI3D. This was conducted only for the vertical intensity ($\mu = 1$), using a small test barium model atom, under the assumption of LTE. We used the same opacity sources and the same input model atmosphere. Systematic differences in the equivalent widths less than 2.2% were found between intensities computed with MULTI 2.3 and intensities computed with MULTI3D. This translates into abundances differences much less than 0.01 dex. The reason for these small differences is likely the way in which each code solves the radiative transfer equation: MULTI3D uses a direct 1D integration of the radiative transfer equation when computing spectra from 1D model atmospheres[3], while MULTI 2.3 uses a faster Feautrier method. However, abundance uncertainties found here are far smaller than the errors we report in Sect. 5. Therefore, we were satisfied that comparing 1D output from MULTI 2.3 with 3D output from MULTI3D was adequate.

We ran MULTI3D in short characteristic 3D solver mode and used the solar STAGGER model as input. The STAGGER model xy grid points were scaled down by a factor of 64 from 240×240 to 30×30 grid points using a simple bilinear interpolation scheme. Significant tests conducted in the first paper in this paper series (Bergemann et al. 2019, henceforth Paper I), revealed no significant loss of information in the horizontal gas flows that affected the line profiles in any noteworthy way. The horizontal components were also assumed to be periodic so that rays with very low μ angles could be computed without encountering horizontal boundaries. The vertical grid size remained consistent with the original model atmosphere at 230 grid points.

2.6. The barium model atom

The model atom of barium was constructed as follows. The energy levels for the Ba I and Ba II levels were extracted from the NIST database. Of these, we included eight energy states of Ba I up to the energy of 2.86 eV, and all available levels of Ba II up to 9.98 eV. Fine structure was retained for the three lowest terms of Ba II: 6s ^{2}S (ground state), 5d ^{2}D (∼0.65 eV), and 6p ^{2}P° (∼2.6 eV) (Table 1). Transitions between these terms are typically used in the barium abundance analysis of cool stars. Other levels were merged into terms, and their energy levels are represented by the weighted sum of the individual components (weighted by the statistical weights of the levels). In total, the model comprises 110 states and is restricted by the ground state of Ba III at 15.2 eV for a total of 111 levels. No lines of Ba I are observed in the spectra of FGK stars. For the Sun, $n_{\rm Ba\,I}/n_{\rm Ba\,II} \approx 10^{-4}$–$10^{-6}$ (see Sect. 3.1), which means that Ba I is a minority species. A detailed treatment of the neutral stage is therefore of no importance to the statistical equilibrium Ba II, which is the majority species in these stars. Figure 2 depicts the energy levels in Ba II and transitions among them in the form of a Grotrian diagram. The model contains too many energy levels to accurately depict without overlapping energy states, therefore this figure should be used for qualitative assessments only.

The radiative bound–bound transitions for Ba II were extracted from the `Kurucz database` on 26 March 2017. We also compared the data with the `NIST database`. For the combined terms, the lines were merged and the transition probabilities co-added as described in Bergemann et al. (2012a). The oscillator strengths of the four diagnostic lines we used were extracted from the experimental transition probabilities presented in the studies by De Munshi et al. (2015) and Dutta et al. (2016). In total, the model contains 284 spectral lines in the wavelength range from 1330 to 202 930 Å. The transitions with $\log gf < -10$ are not included. Most of these lines are represented by nine frequency points, except for the four diagnostic lines that we used in the abundance analysis, that is, the lines at 4554, 5853, 6141, and 6496 Å. These lines were represented with a profile containing 301 frequency points. Several UV lines

[3] Ordinarily, MULTI3D uses a short characteristic solver for 3D model atmospheres.

Table 1. Ba II lines used in the abundance analysis of the Sun.

Wavelength (Å)	Elow (eV)	Eup (eV)	Conf.	Conf.	log gf	VdW	EW (mÅ)
4554.033	0.00	2.72	$6s\,^2S_{0.5}$	$6p\,^2P^\circ_{1.5}$	0.170 ± 0.004	303.222	207
5853.675	0.60	2.72	$5d\,^2D_{1.5}$	$6p\,^2P^\circ_{1.5}$	−1.023 ± 0.005	365.264	68
6141.713	0.70	2.72	$5d\,^2D_{2.5}$	$6p\,^2P^\circ_{1.5}$	−0.070 ± 0.005	365.264	126
6496.898	0.60	2.51	$5d\,^2D_{1.5}$	$6p\,^2P^\circ_{0.5}$	−0.365 ± 0.004	365.264	102

Notes. The wavelengths are given in air. The equivalent widths correspond to the measurements in the solar KPNO flux atlas and are given in mÅ. The Van der Waals broadening parameters are taken from Barklem et al. (2000). The log gf values reported here are derived from the very accurate transition probabilities taken from De Munshi et al. (2015) and Dutta et al. (2016).

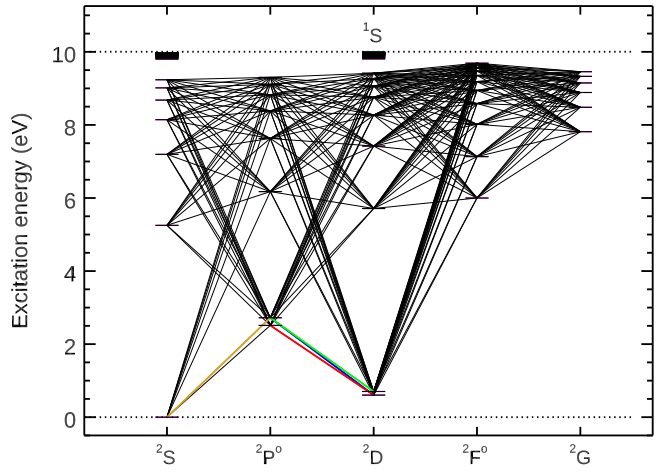

Fig. 2. Grotrian diagram of the Ba II atom. Gold, green, blue, and red lines indicate the diagnostic Ba II lines that we use in the solar abundance analysis at 4554, 5853, 6141, and 6496 Å, respectively.

are rather strong. To test whether nine frequencies were enough to describe these strong lines, we ran a test using MULTI 2.3. The departure coefficients from the model atom were compared with an atom that contained 100 frequency points for two strong UV transitions at 2304.247 and 2341.429 Å. It was found that these transitions have no effect on the populations of the four barium lines of interest. This justifies the number of frequency points chosen for transitions that were not of interest to us for this study. Damping by elastic collisions with hydrogen atoms were computed using the α and σ parameters from Barklem et al. (2000) where available. When this information was missing, we used the Unsöld approximation, which was scaled by 1.5. The wavelengths were taken from Karlsson & Litzén (1999). We found that three lines (not the line at 4554 Å) were systematically offset from the solar spectrum. When the solar spectrum was corrected for gravitational redshift, they did match the observed line positions, although the 4554 Å resonance line has a slightly different shift. Karlsson & Litzén underlined that this line might be slightly shifted in their measurements as a result of the isotopic mix they used and self-absorption in this strong line. This shift is expected to be at most 1 mÅ to the blue (Litzén, priv. comm.), however, which is not sufficient to explain the remaining offset we observe. We discovered that the excess shift in this line was due to convective effects. We shifted the 4554 Å line by 2 mÅ in 1D to the blue to match the observed position, but we did not need to shift the 3D profile.

We also introduced HFS and isotopic shifts. They were computed using the solar abundance ratios of the five barium isotopes, see Eugster et al. (1969). The odd barium isotopes have non-zero nuclear spins that cause hyperfine splitting of the levels. The magnetic dipole and electric quadrupole constants for the five relevant energy levels were taken from Silverans et al. (1986) and Villemoes et al. (1993). The isotopic shifts are provided by van Hove (1982) for the 5853 and 6141 Å lines, by Villemoes et al. (1993) for the 6496 Å line, and by Wendt et al. (1984) for the 4554 Å line. The diagnostic lines are therefore represented by 6–15 HFS components. The complete HFS information for these lines can be found in the tables in Appendix A. Oscillator strengths for these lines were computed from accurate experimental transition probabilities in De Munshi et al. (2015) and Dutta et al. (2016).

The radiative bound-free data were computed using the standard hydrogenic approximation (Kramer's formula). This is appropriate because the first ionisation potential of Ba II is at 10 eV, and the energy levels that may contribute to radiative over-ionisation at the solar flux maximum have very low population numbers. Moreover, on the basis of earlier studies with strontium (Bergemann et al. 2012b), which has a similar atomic structure, we do not expect that photo-ionisation is a significant non-LTE effect. Earlier studies of barium in non-LTE showed that Ba II is a majority ion and is collision dominated (see Mashonkina et al. 1999; Gehren et al. 2001; Bergemann & Nordlander 2014). In such ions, the statistical equilibrium is established by a competition of collisional thermalisation, photon losses in strong lines, and over-recombination. This isdiscussed in detail in the next section.

One of the new features of our atom compared to the earlier studies mentioned above is the treatment of collisions. In particular, we included the new quantum-mechanical rate coefficients for the inelastic collisions between the Ba II ions and hydrogen atoms by Belyaev & Yakovleva (2017, 2018). To the best of our knowledge, the first study of barium that employs these detailed quantum-mechanical data for collisions with hydrogen was recently published by Mashonkina & Belyaev (2019) for the purposes of treating isotopes. In the present paper, these hydrogen-collision data are employed for the first time for full non-LTE modelling. The data are available for 686 processes, and represent collisional excitation and charge transfer reactions, that is, $Ba + H \leftrightarrow Ba^+ + H^-$. The rate coefficients are typically large and may exceed 10^{-8} cm^{3}s^{-1} in the temperature regime relevant to modelling the solar atmosphere. The process ionisation refers to the ion we are interested in and a free electron, that is, ionisation: Ba II + H → Ba III + H + e, but the process ion-pair formation reads Ba II + H → Ba III + H^-, that is, Ba II loses its outer electron and it is bound with H. Its inverse process, mutual neutralisation, is the process when Ba III gains an electron from H^-. The same is valid when Ba II is replaced by Ba I and Ba III

is replaced by Ba II. Charge transfer reactions do not lead to a free electron, which is the case that is usually modelled by Drawin's formula (Drawin 1968, 1969). Excitation and ionisation by collisions with free electrons were computed using the van Regemorter (1962) and Seaton (1962) formulae. A study of the effect of different collisional rates was presented in Andrievsky et al. (2009, Sect. 3.2). No differences between these classical recipes were found. An earlier version of this model atom was used by Eitner et al. (2019). We have since updated the oscillator strengths.

3. Barium line formation

3.1. Non-LTE effects

In terms of departures from LTE, Ba II is a collision-dominated ion (see Gehren et al. 2001, and references therein). The ionisation potential is too high for photo-ionisation to play a significant role in the statistical equilibrium (SE) in FGK type stars. On the other hand, the term structure of the ion, with several very strong radiative transitions, favours strong effects caused by line scattering. In particular, there is radiative pumping at the frequencies of optically thin line wings, $\tau_{\rm wing} < 1$, as long as at the line centre $\tau_{\rm core} > 1$. This mechanism acts predominantly at larger depths and leads to over-population of the upper levels of the transitions, at the expense of the lower states. On the other hand, strong downward cascades occur higher up in the atmosphere, where the strong line cores become optically thin, $\tau_{\rm core} < 1$. This mechanism de-populates the upper levels through spontaneous de-excitations, and this downward electron cascade causes over-population of the lower lying energy states. As the statistical equilibrium of Ba II has been extensively studied in the literature (Mashonkina & Bikmaev 1996; Mashonkina et al. 1999, 2008; Short & Hauschildt 2006), in what follows we only describe the main features of the non-LTE line formation and discuss the differences with the earlier studies.

Quantitatively, this behaviour can be visualised as plots of the departure coefficients b_i[4] as a function of the continuum optical depth at 5000 Å, $\log \tau_{5000}$. Figure 3 depicts the b_i behaviour for the solar MARCS model atmosphere. To facilitate the comparison with the detailed study by Mashonkina et al. (1999), we chose the same axis range as was used in that paper. Thick coloured curves correspond to the five energy states that are involved in the radiative transitions listed in Table 1: the ground state of Ba II, 6s ^{2}S, and the low-excitation terms 5d ^{2}D and 6p ^{2}P°. Thin grey dotted curves show all other energy levels of Ba II in the model atom. It is interesting that despite large differences in the model and numerical methods, including the properties of the atomic model, model atmosphere, and the SE code, the agreement between our results and that of Mashonkina et al. (1999, see their Fig. 2) is very good. In particular, the Ba II ground state is entirely thermalised throughout the full optical depth range and develops a very modest over-population only at $\log \tau_{5000} < -4$. The first excited metastable state 5d ^{2}D is also close to LTE due to strong collisional coupling with the Ba II ground state, although minor departures in the atomic number densities, of about a few percent, are seen at $\log \tau_{5000} < -3$ and higher up. The term 6p ^{2}P° at ~2.6 eV shows stronger deviations from LTE already in the deep layers, $\log \tau_{5000} \sim -2$, where the non-LTE population of the level is only about 80% of the LTE

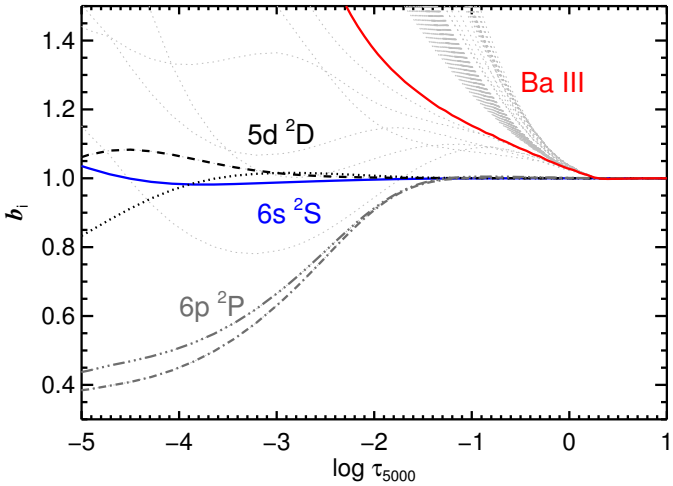

Fig. 3. Departure coefficients for the Ba II levels as a function of the continuum optical depth $\log \tau_{5000}$ computed using the reference barium model atom for the solar MARCS model atmosphere.

value (i.e. equivalent to $b_i = 0.8$). The pronounced depletion of the term is caused by photon losses in the lines, connecting the ground state and the lowest metastable state with 6p ^{2}P°. This under-population increases outwards as the lines become optically thin. All energy levels above 6p ^{2}P° are over-populated at $\log \tau_{5000} < 0$. This effect was attributed by Mashonkina et al. (1999) to radiative pumping.

It is interesting to briefly discuss the importance of microphysical processes in the SE of Ba II. Andrievsky et al. (2009) suggested that photo-ionisation cross-sections are the main source of uncertainty in the SE of Ba II. This is only true for Ba I, however. No lines of the neutral atom are observed in the optical or infra-red spectra of FGKM stars (Tandberg-Hanssen 1964). Over-ionisation of Ba I has no effect on the population of Ba II because the ratios of number densities of two ionisation stages are $n_{\rm BaI}/n_{\rm BaII} \sim 10^{-4}$ at $\log \tau_{5000} \approx 0$, and this drops to $\sim 10^{-6}$ in the outermost atmospheric layers in the solar model. This ratio is even more extreme in the atmospheres of metal-poor stars. For example, for a model atmosphere of an RGB star with $T_{\rm eff} = 4600$ K, $\log g = 1.6$, and [Fe/H] = −2.5, $n_{\rm BaI}/n_{\rm BaII} \sim 10^{-5}$ at $\log \tau_{5000} \approx 0$, but approaches $\sim 10^{-10}$ close to the outer boundary at $\log \tau_{5000} \approx -5$. On the other hand, photo-ionisation in Ba II is not important. The ion has a very high ionisation potential, and its well-populated energy levels with low excitation potentials have ionisation thresholds in the far-UV, at $\lambda < 1000$ Å, where radiative flux in FGK-type stars is negligibly low. We also recomputed the departure coefficients assuming $\sigma_{\rm photo}/100$ and $\sigma_{\rm photo} \times 100$. This is a very conservative uncertainty estimate in the cross-sections when compared to those of a very similar atom, Sr, for which detailed quantum-mechanical cross-sections are available from Bergemann et al. (2012a). It was found that only the non-LTE populations of the Ba III ground state change, but none of the important Ba II levels show any difference with respect to our reference model.

A more important ingredient for the SE of Ba II seems to be the accuracy of the data for inelastic collisional processes, in particular, those between Ba II and H I atoms. Short & Hauschildt (2006) suggested that the non-LTE line profiles are invariant to changes of a factor 0.1−10 in the rates of transitions that are caused by collisions (they used approximate analytical formulae to represent these data). This may hold for a limited range of stellar parameters. For example, in the case of the Sun, using

[4] The departure coefficient is defined as the ratio of atomic number density for a given energy level i computed in non-LTE to that of LTE, $b_i = \frac{n_{i,\rm non-LTE}}{n_{i,\rm LTE}}$.

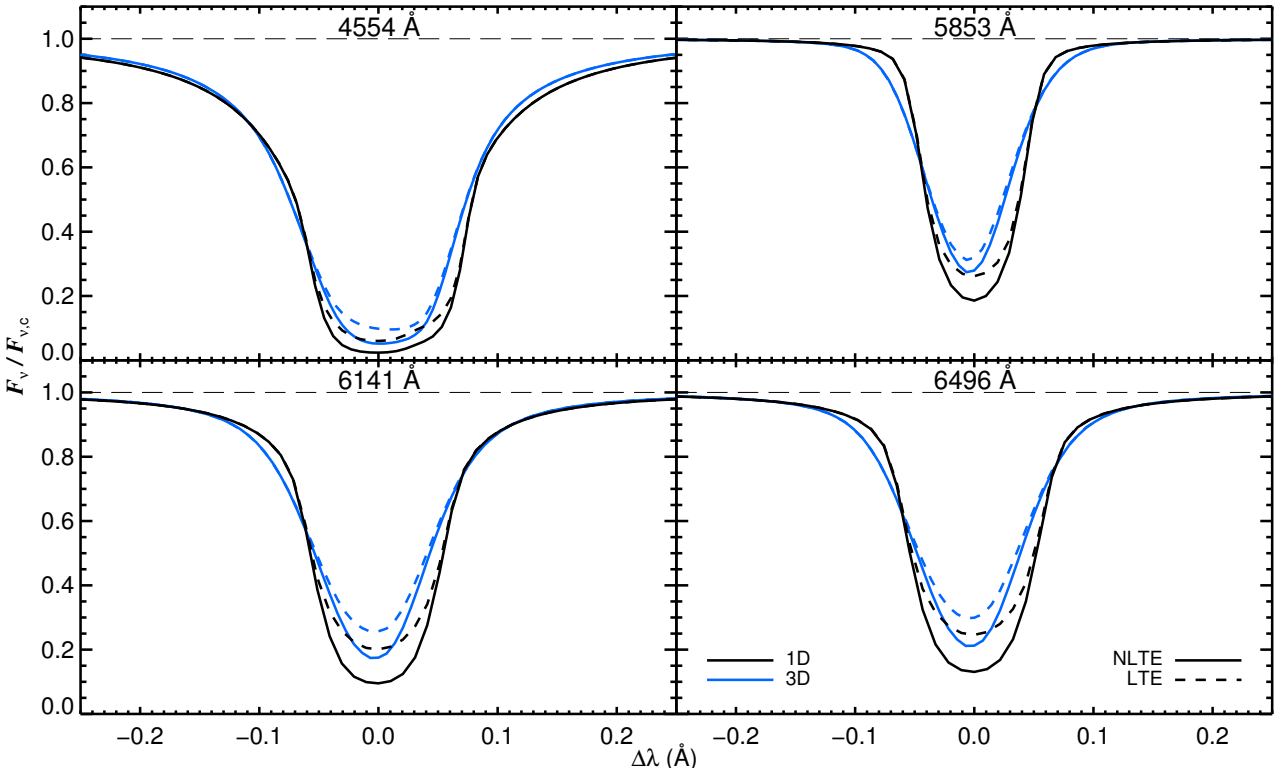

Fig. 4. Ba II line profiles at A(Ba) = 2.26 dex in 1D (black), 3D (blue), LTE (dashed lines), and non-LTE (solid-lines). No additional broadening was added to any of the depicted lines. The 3D profiles are shown to be shifted relative to the 1D profiles. This is a natural consequence of the convective shifts that are indicative of a dynamic model atmosphere.

Drawin's recipe or QM data does not give significantly different results. However, it is known that metal-poor stars are sensitive to non-LTE effects (Bergemann & Nordlander 2014). Therefore, it would be reasonable to assume that they would also be sensitive to different collisional recipes. This is particularly true in hydrodynamic model atmospheres because the decoupled non-local radiation field leads to a cooling in the outer regions of the temperature structure relative to the equivalent 1D model (see e.g. Gallagher et al. 2016, their Fig. 1). We intend to explore this in the near future.

3.2. Line formation in hydrostatic and inhomogeneous models

We begin with the analysis of LTE and non-LTE formation of Ba II lines in the 1D hydrostatic solar model. We then extend the analysis to radiative transfer with 3D inhomogeneous models.

As discussed in the previous section, the non-LTE effects in Ba II are primarily dominated by line scattering. Consequently, deviations from LTE in the line source function are expected to be significant. Because the ratio of the departure coefficients for the lower i and upper j level of the transitions is below unity for the diagnostic Ba II lines, $b_j/b_i < 1$, the ratio of source function to the Planck function (see Bergemann & Nordlander 2014, for the derivation) also drops below unity. In other words, the source function in the line is sub-Planckian and the non-LTE lines profiles come out stronger than the LTE lines. In some cases (e.g. Bergemann et al. 2012a, for Sr), this effect is modulated by the change of the line opacity. However, because $\kappa_\nu \sim b_i$ and the population numbers for the lower levels of all Ba II lines are essentially thermal throughout the line formation depths, the line opacity is very close to its LTE value. This simple analytical picture is confirmed by comparing the LTE and non-LTE line profiles (Fig. 4). The non-LTE effects are small and amount to the abundance difference of −0.05 (4554 Å) to −0.1 dex (5853 Å). The other two Ba II lines show a similar behaviour.

Figure 4 demonstrates that the 3D profiles are asymmetric and also shifted blueward relative to the 1D profiles, which is expected. This is a natural result of the convective motions inside the 3D model that the 1D model cannot replicate (Löhner-Böttcher et al. 2018; Stief et al. 2019). This is particularly obvious in the three subordinate lines, where the HFS has a far weaker effect on the line shape than it does on the resonance line, where asymmetries are seen in both 1D and 3D. The 3D profiles for a given barium abundance are consistently weaker than their 1D counterparts, both in LTE and non-LTE. Therefore, positive abundance corrections are required to reproduce the same equivalent width, foreshadowing larger 3D LTE and non-LTE abundances over the 1D LTE counterpart. As we showed in the hydrostatic case above, deviations from LTE are expected to be significant because of line scattering.

The lines of Ba II in the solar spectrum are strong, with equivalent widths (EWs) from 207 (4554 line) to 68 mÅ (5853 Å) line. They are therefore not only extremely affected by damping, but are also blended. The 4554 Å line is blended by a Fe II feature close the line core, but has little effect on the line. The subordinate lines also show some blending. Korotin et al. (2015) avoided the 4554 Å line in particular in their analysis of FGK metal-poor stars in stars where [Fe/H] > −1.0. On the other hand, Grevesse et al. (2015) included the 4554, 5853, and 6496 Å lines in their analysis of the Sun. They also used the non-LTE corrections for Ba II lines. We explore the effects of line blending and damping in Sect. 5.

The current photospheric solar abundance of barium derived by Grevesse et al. (2015), who applied non-LTE corrections to

Table 2. 1D non-LTE, 3D LTE, and 3D non-LTE abundance corrections, Δ.

Wavelength (Å)	$\Delta_{\rm 1D\,NLTE}$	$\Delta_{\rm 3D\,LTE}$	$\Delta_{\rm 3D\,NLTE}$
4554.033	−0.05	0.11	0.08
5853.673	−0.11	0.05	0.03
6141.711	−0.15	0.10	0.04
6496.896	−0.19	0.10	0.02

Notes. Corrections are defined as $\Delta_D = A(\mathrm{X})_D - A(\mathrm{X})_{\rm 1D\,LTE}$, where D is the 3D non-LTE, 3D LTE, or 1D non-LTE case.

their 3D LTE abundance, is 2.25 ± 0.03 ± 0.07 (where errors represent the statistical and systematic errors, respectively). The abundance of barium in CI meteorites (Lodders 2003) is 2.19 ± 0.03. The main goal of this paper is to explore whether ab initio atomic data from physical experiments and detailed quantum-mechanical calculations are successfully able to describe the spectrum of the Sun. Accordingly, we now report our 1D non-LTE, 3D LTE, and 3D non-LTE corrections relative to the average barium 1D LTE abundance.

4. Computing abundance corrections

A grid of abundances for all four barium lines was computed using MULTI 2.3. These were fit to the solar spectrum using a χ^2 code that treats abundances, macroturbulent broadening, and wavelength shifts as free parameters (see Sect. 2.6 for details of the line shifts). The macroturbulences we found ranged from 1.5−1.9 km s^{-1}. The code also normalises the fit to a local continuum for each line using two patches of spectrum either side of the line. We fixed the rotational broadening to $v \sin i$ = 1.6 km s^{-1} (Pavlenko et al. 2012). The 1D LTE we obtain represents the best statistical fit from this χ^2 code.

We computed the four barium lines in 1D non-LTE, 3D LTE, and 3D non-LTE using three abundances: A(Ba) = 2.17, 2.27, and 2.35. This covers the typical abundances reported in the literature for the solar barium abundance. The abundance corrections tabulated in Table 2 were determined by fitting the grid of 1D LTE profiles to the 1D non-LTE, 3D LTE, and non-LTE lines so that their EWs matched. The corrections from all three abundances were identical, as expected. The corrections we provide are therefore robust against the typical abundance range found by most studies on the solar barium abundance.

5. Results

Our best-fit profiles were compared with the solar flux profiles in Fig. 5. The best-fit 3D lines were computed by MULTI3D using the corrections given in Table 2. The 3D non-LTE abundances are remarkably consistent, except for the 6141 Å line, which is approximately 0.12 dex larger than the other three. The reasons for this are explained at the end of this section. Unlike in the 1D case, the best-fit 3D LTE profiles show large deviations in the line cores relative to their non-LTE counterparts, but their EWs remain very similar.

The lines and abundances discussed this far have assumed that the barium lines are unblended in the solar spectrum. In reality, this is not the case. The abundances of all barium lines (particularly the 6141 Å line) are dependent on line blending, as we discuss now.

5.1. Line blending corrections

The four barium lines we modelled here suffer from the effects of blending with other atomic and molecular species. This affects the abundances we derive when we assume that the line is clean. This was done when we synthesised the lines with MULTI3D and MULTI 2.3 because these codes do not currently possess the capability to synthesise blends. To examine this, we used the VALD3[5] database together with the barium line information extracted from the model atom to create new line lists for the 1D LTE spectrum synthesis code MOOG[6]. This code was chosen because the interactive plotting tool facilitates recomputing synthetic spectra and fitting them with observed data simple. Lines were computed with and without blends and the abundance of the unblended barium line was adjusted until its line strength matched that of the blended line.

The Ba II resonance line at 4554 Å is the strongest line presented here. It would dominate most of the line depression in this spectral region. When blends are included, the 1D LTE barium abundance must be reduced by 0.01 dex. The 5853 Å line abundance was reduced by 0.03 dex. The 6141 Å line was found to be severely affected by blending because the abundance had to be reduced by 0.16 dex. The 6496 Å barium abundance had to be reduced by 0.04 dex.

We use these abundance corrections to determine the barium abundance in all four paradigms in Sect. 5.4. First, however, it is important to determine how the barium lines are affected by systematic uncertainties, which we present now.

5.2. Line damping uncertainties

We previously mentioned that differences in the radiative transfer solvers used by MULTI 2.3 and MULTI3D lead to extremely small systematic uncertainties in the barium abundance. These are small (<0.01 dex) enough to be dwarfed by the uncertainties associated with the van der Waals broadening parameters that we discuss now. The barium lines we synthesised here have varying line strengths. This means that they will react differently to uncertainties associated with the van der Waals line damping parameters σ and α. When we conservatively assume a 10% uncertainty associated with the damping parameters tabulated in Barklem et al. (2000), then we can see how this affects the abundance measured in each line and derive a systematic uncertainty for each line. This does not affect the abundance corrections because these systematics will affect all syntheses equally and so they cancel out, but it is important to determine any uncertainty associated with the abundances determined from these corrections.

We examined how the cross sections (σ) and velocity exponent (α) affect the line strength by varying both separately and computing new lines using MULTI 2.3. Varying α by ±10% had no impact on the line strengths of any of the lines, and we therefore cannot attribute any abundance uncertainty to this parameter. However, a 10% uncertainty in σ was found to affect the line strength in all four lines. The 4554 Å line is the strongest measured line (207 mÅ). It is therefore reasonable to assume that this line is most affected by this damping parameter uncertainty. The barium abundance determined from this line varies by ±0.03 dex. The 5853 Å line is the weakest line in this study (68 mÅ). The uncertainty we assign to the van der

[5] http://vald.astro.uu.se/
[6] https://www.as.utexas.edu/~chris/moog.html

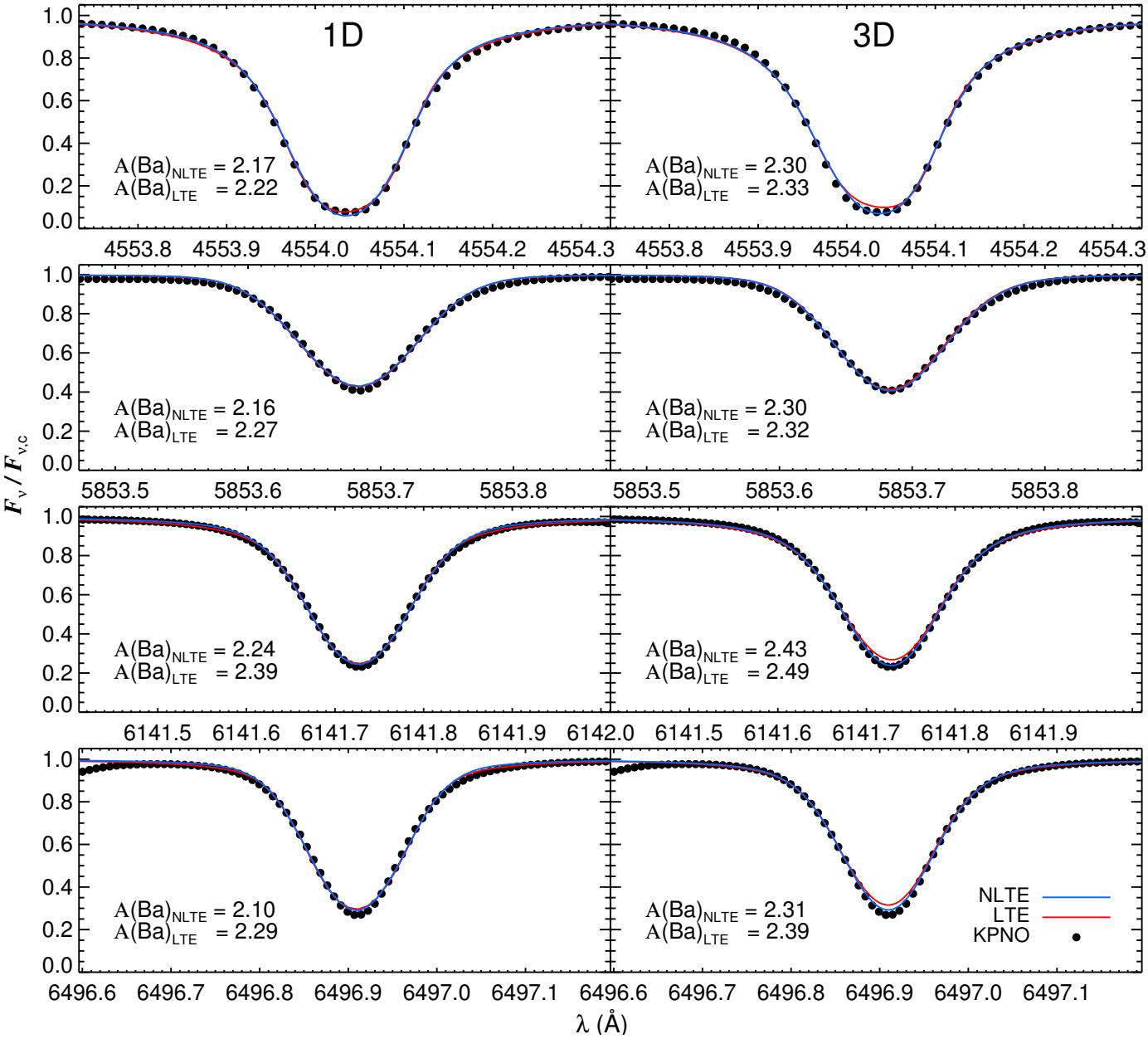

Fig. 5. Best-fit Ba II lines in 1D (*left panels*) and 3D (*right panels*) for the LTE (red) and non-LTE (blue) cases. The 3D and 1D non-LTE profiles were computed using Table 2. Abundances provided in the panels do not represent the final barium abundance because line blends are excluded here. See Sect. 5 and Table 3 for details.

Waals parameter of ±10% therefore leads to a change in abundance of only 0.01 dex. The 6141 Å line is the second strongest measured line (126 mÅ). This leads to abundance variations of ±0.03 dex. Finally, the 6496 Å line is also fairly strong in the solar spectrum (102 mÅ). The uncertainty we assign the damping parameter varies the barium abundance we found in this line by ±0.02 dex. The list of associated abundance uncertainties is shown in Col. 4 of Table 3.

Uncertainties in line blends are also of concern when abundances are computed. No uncertainty information is given in the VALD database, therefore we again conservatively assumed that the $\log gf$ values of these lines have a 10% uncertainty. The abundances obtained from the 4554 Å line with and without line blending were virtually identical. As previously mentioned, this is because the resonance line dominates line depression in this spectral region. Accordingly, uncertainties in blended lines of ±10% do not affect the barium abundance. While the 5853 Å line is the weakest analysed line, it suffers least from blending. This shows that no sensitivity in barium abundance is found from varying the blended lines either. The blends around the 6141 Å line have a strong effect on the barium abundance. Uncertainties in $\log gf$ lead to an uncertainty of ±0.02 dex. Therefore, the inclusion of blend uncertainties increases the systematic uncertainty of the 6141 Å from 0.03 dex to 0.04 dex. Finally, the blending uncertainties around the 6496 Å line were not found to influence the barium abundance. A break-down of the associated abundance uncertainties is shown in Col. 5 of Table 3.

5.3. Oscillator strength uncertainties

The oscillator strengths (f-value) of the four diagnostic lines we used were taken from De Munshi et al. (2015) and

Table 3. Abundances, associated error estimates, and abundance corrections due to line blending.

							LTE		non-LTE	
Wavelength (Å)	$A(\mathrm{Ba})_{\mathrm{1D,LTE}}$	Δ_{blend}	σ_{BPO}	σ_{blends}	$\sigma_{f-\mathrm{value}}$	σ_{total}	$A(\mathrm{Ba})_{\mathrm{1D}}$	$A(\mathrm{Ba})_{\mathrm{3D}}$	$A(\mathrm{Ba})_{\mathrm{1D}}$	$A(\mathrm{Ba})_{\mathrm{3D}}$
4554.033	2.22	−0.01	±0.03	±0.00	±0.00	±0.03	2.21	2.32	2.16	2.29
5853.673	2.27	−0.03	±0.01	±0.00	±0.01	±0.01	2.24	2.29	2.13	2.27
6141.711	2.39	−0.16	±0.03	±0.02	±0.01	±0.04	2.23	2.33	2.08	2.27
6496.896	2.29	−0.04	±0.02	±0.00	±0.01	±0.02	2.25	2.35	2.06	2.27

Notes. Column 2 tabulates the 1D LTE abundances found when the lines were assumed to be clean. They are consistent with the profiles depicted in Fig. 5. Column 3 presents the abundance correction associated with line blending. The final four columns present actual abundances of each line when the appropriate corrections were added to Cols. 2 and 3 from Table 2. The weighted averages calculated in Sect. 5.4 are computed using these abundances and the systematic errors tabulated in Col. 7 from the errors in BPO theory (Barklem et al. 2000), line blend uncertainties, and oscillator strengths, f, which are presented in Cols. 4, 5, and 6, respectively.

Dutta et al. (2016). They also provide unique errors associated with each transition probability, which we converted into oscillator strength uncertainties. The transition probabilities are extremely accurate, therefore the resulting uncertainties are very small. When these were included in our calculations, we found that the propagated abundance error associated with the 4554 Å line is ±0.00 dex. The weakest line in our sample (5853 Å) has a propagated abundance uncertainty of ±0.01 dex. The most strongly blended line (6141 Å) is found to have a propagated abundance uncertainty of ±0.01 dex. Finally, the 6496 Å line has an associated abundance error of ±0.01. The associated abundance uncertainties for each line are shown in Col. 6 of Table 3.

5.4. Solar barium abundance

We now present the barium abundance in four paradigms: 3D non-LTE, 3D LTE, 1D non-LTE, and 1D LTE. We corrected the 1D LTE abundances using the corrections in Table 2 and Sect. 5.1, and weighted them by their uncertainties listed in Table 3 using an inverse-variance weighted mean ($\sum \omega_i X_i$, where $\omega_i = \frac{1}{\sigma^2}$).

We report for the first time a full 3D non-LTE solar barium abundance of 2.27 ± 0.02 ± 0.01, where errors given here are the systematic uncertainties and the random error determined as the standard deviation found in the line-to-line scatter of the 3D non-LTE abundances, which is also shown in Table 3. This value is 0.08 dex larger than the meteoritic barium abundance of 2.19 ± 0.03 determined by Lodders (2003). We therefore find a photospheric abundance that is slightly larger than that reported from meteorites.

Using the same method as described above, we find that $A(\mathrm{Ba}) = 2.31 \pm 0.02 \pm 0.03$ in 3D LTE. Errors again represent the systematic and random errors. When we used 1D model atmospheres and applied non-LTE physics to the post-process spectral synthesis, we found that the 1D non-LTE barium abundance is $A(\mathrm{Ba}) = 2.11 \pm 0.02 \pm 0.05$. Finally, when we derived the barium abundance using the classical 1D LTE approach, we found that $A(\mathrm{Ba}) = 2.24 \pm 0.02 \pm 0.02$. This abundance is similar to the 3D non-LTE abundance.

6. Conclusions

We have computed new values of the solar barium abundance based upon results that were computed using a new barium model atom that includes quantum-mechanical inelastic collisional rate coefficients between Ba II and hydrogen. We computed the barium abundance using a static 1D model atmosphere and provide 1D non-LTE, 3D LTE, and 3D non-LTE corrections to this value in Table 2. Using these corrections, we also present new solar photospheric barium abundances for the first time in full 3D non-LTE, as well as in 3D LTE, 1D non-LTE, and 1D LTE. The summary of this work is listed below (to all abundances given below, the corrections to each 1D LTE abundance were added and then the inverse-variance weighted mean was derived as described in Sect. 5.4).

- The 3D non-LTE barium abundance was found to be $A(\mathrm{Ba}) = 2.27 \pm 0.02 \pm 0.01$, which is 4σ larger the meteoritic abundance published by Lodders (2003). This may suggest uncertainties in the atomic data and/or that further physics is still missing from our analyses, such as the treatment of magnetic fields. On the other hand, Ba isotopic abundance anomalies are well documented in CI meteorites (e.g. McCulloch & Wasserburg 1978; Arnould et al. 2007), and it is not clear whether the meteoritic value can indeed be directly compared to the solar photospheric estimate. Nevertheless, this value represents the best photospheric solar barium abundance available from current state-of-the-art spectral modelling. As a result, it provides a remarkably consistent abundance for the four diagnostic lines.
- The 3D LTE abundance was determined as $A(\mathrm{Ba}) = 2.31 \pm 0.02 \pm 0.03$. This value is larger than the meteoritic value given in Lodders and the 3D non-LTE abundance we determine, and the individual abundances are not as consistent.
- The 1D non-LTE abundance of $A(\mathrm{Ba}) = 2.11 \pm 0.02 \pm 0.05$ suggests that the barium abundance is depleted by 0.16 dex in the solar atmosphere relative to the full 3D non-LTE. The abundance is also less than the meteoritic result reported in Lodders and the inconsistencies between lines are larger than they are in 3D non-LTE.

The 3D non-LTE and 1D LTE abundances are very similar for barium in the Sun, but larger than that given in Lodders (2003). Conversely, the 3D LTE abundance suggests that the barium abundance is even larger in the Sun, while the 1D non-LTE abundance suggests that barium is slightly lower than the meteoritic value. It is clear then that the inclusion or removal of realistic treatments of line formation physics or convection has opposite effects on the barium abundance: the former strengthens the barium lines and so depletes the barium abundance, while the latter weakens the barium lines and hence a larger barium abundance is required. Therefore, the exclusion of both physical processes in the 1D LTE paradigm masks each effect, providing similar values in each line as the actual values found in 3D non-LTE. Conversely, in our work on manganese, we found that the 3D and non-LTE effects do not cancel out, but that the

effects of non-LTE are instead amplified in 3D calculations with hydrodynamical models.

The previous set of transition probabilities reported by Davidson et al. (1992) led to abundances values that were, in general, less consistent than those reported here and had larger uncertainties associated with them, with the 5853 Å line being most uncertain and most inconsistent with the other three diagnostic lines. The latest published transition probabilities in De Munshi et al. (2015) and Dutta et al. (2016) represent the most accurate transition parameters published. The barium abundances we find from each diagnostic line used here therefore all agree very well (when the blending corrections are included).

We have presented this work as part of a larger series of papers designed to report on the development of the MULTI3D spectrum synthesis code. We have added new coding that allows the code to read standard STAGGER model atmospheres, to include the effect of charge transfer between hydrogen and ions, to compute flux data based on hard-coded quadrature schemes, and to compute multi-component transitions caused by HFS or isotope splittings. Further physics and mathematical techniques will be added as the project progresses. This will be presented in future papers in this paper series. We also plan to extend our work on barium within this paper series to include several metal-poor benchmark stars, where the present work will be important to the relative abundances we report.

Acknowledgements. This work made heavy use of the Max Planck Computing & Data Facility (MPCDF) for the majority of the computations. This project was funded in part by Sonderforschungsbereich SFB 881 "The Milky Way System" (subproject A5) of the German Research Foundation (DFG) and by the Research Council of Norway through its Centres of Excellence scheme, project number 262622. S.A.Y. and A.K.B. gratefully acknowledge support from the Ministry for Education and Science (Russian Federation), project Nos. 3.5042.2017/6.7, 3.1738.2017/4.6. B.P. is partially supported by the CNES, Centre National d'Etudes Spatiales.

References

Abramowitz, M., & Stegun, I. A. 1972, Handbook of Mathematical Functions (Gaithersburg, MD: United States Department of Commerce, National Institute of Standards and Technology)
Amarsi, A. M., & Asplund, M. 2017, MNRAS, 464, 264
Amarsi, A. M., Asplund, M., Collet, R., & Leenaarts, J. 2016, MNRAS, 455, 3735
Andrievsky, S. M., Spite, M., Korotin, S. A., et al. 2009, A&A, 494, 1083
Arlandini, C., Käppeler, F., Wisshak, K., et al. 1999, ApJ, 525, 886
Arnould, M., Goriely, S., & Takahashi, K. 2007, Phys. Rep., 450, 97
Asplund, M., Nordlund, Å., Trampedach, R., Allende Prieto, C., & Stein, R. F. 2000, A&A, 359, 729
Asplund, M., Carlsson, M., & Botnen, A. V. 2003, A&A, 399, L31
Barklem, P. S., Piskunov, N., & O'Mara, B. J. 2000, A&AS, 142, 467
Belluzzi, L., & Trujillo Bueno, J. 2013, ApJ, 774, L28
Belyaev, A. K., & Yakovleva, S. A. 2017, A&A, 608, A33
Belyaev, A. K., & Yakovleva, S. A. 2018, MNRAS, 478, 3952
Bergemann, M., & Nordlander, T. 2014, ArXiv e-prints [arXiv:1403.3088]
Bergemann, M., Hansen, C. J., Bautista, M., & Ruchti, G. 2012a, A&A, 546, A90
Bergemann, M., Lind, K., Collet, R., Magic, Z., & Asplund, M. 2012b, MNRAS, 427, 27
Bergemann, M., Gallagher, A. J., Eitner, P., et al. 2019, A&A, 631, A80 (Paper I)
Carlsson, M. 1986, A Computer Program for Solving Multi-level Non-LTE Radiative Transferproblems in Moving or Static Atmospheres (Uppsala, Sweden: Uppsala Astronomical Observatory Reports), 33
Collet, R., Magic, Z., & Asplund, M. 2011, J. Phys. Conf. Ser., 328, 012003
Davidson, M. D., Snoek, L. C., Volten, H., & Doenszelmann, A. 1992, A&A, 255, 457
De Munshi, D., Dutta, T., Rebhi, R., & Mukherjee, M. 2015, Phys. Rev. A, 91, 040501
Drawin, H.-W. 1968, Z. Phys., 211, 404
Drawin, H. W. 1969, Z. Phys., 228, 99
Dutta, T., de Munshi, D., Yum, D., Rebhi, R., & Mukherjee, M. 2016, Sci. Rep., 6, 29772
Eitner, P., Bergemann, M., & Larsen, S. 2019, A&A, 627, A40
Eugster, O., Tera, F., & Wasserburg, G. J. 1969, J. Geophys. Res., 74, 3897
Gallagher, A. J., Ryan, S. G., García Pérez, A. E., & Aoki, W. 2010, A&A, 523, A24
Gallagher, A. J., Ryan, S. G., Hosford, A., et al. 2012, A&A, 538, A118
Gallagher, A. J., Ludwig, H.-G., Ryan, S. G., & Aoki, W. 2015, A&A, 579, A94
Gallagher, A. J., Caffau, E., Bonifacio, P., et al. 2016, A&A, 593, A48
Gehren, T., Butler, K., Mashonkina, L., Reetz, J., & Shi, J. 2001, A&A, 366, 981
Gigas, D. 1988, A&A, 192, 264
Grevesse, N., Asplund, M., & Sauval, A. J. 2007, Space Sci. Rev., 130, 105
Grevesse, N., Scott, P., Asplund, M., & Sauval, A. J. 2015, A&A, 573, A27
Gudiksen, B. V., Carlsson, M., Hansteen, V. H., et al. 2011, A&A, 531, A154
Gustafsson, B., Edvardsson, B., Eriksson, K., et al. 2008, A&A, 486, 951
Hayek, W., Asplund, M., Carlsson, M., et al. 2010, A&A, 517, A49
Karlsson, H., & Litzén, U. 1999, Phys. Scr, 60, 321
Klevas, J., Kučinskas, A., Steffen, M., Caffau, E., & Ludwig, H.-G. 2016, A&A, 586, A156
Kobanov, N. I., Chupin, S. A., & Kolobov, D. Y. 2016, Astron. Lett., 42, 55
Korotin, S. A., Andrievsky, S. M., Hansen, C. J., et al. 2015, A&A, 581, A70
Kostik, R., Khomenko, E., & Shchukina, N. 2009, A&A, 506, 1405
Kurucz, R. L., Furenlid, I., Brault, J., & Testerman, L. 1984, Solar flux atlas from 296 to 1300 nm (New Mexico: National Solar Observatory)
Leenaarts, J., & Carlsson, M. 2009, ASP Conf. Ser., 415, 87
Lodders, K. 2003, ApJ, 591, 1220
Löhner-Böttcher, J., Schmidt, W., Stief, F., Steinmetz, T., & Holzwarth, R. 2018, A&A, 611, A4
Lowan, A. N., Davids, N., & Arthur, L. 1942, Bull. Am. Math. Soc., 48, 739
Magain, P. 1995, A&A, 297, 686
Magain, P., & Zhao, G. 1993, A&A, 268, L27
Magic, Z., Collet, R., Asplund, M., et al. 2013, A&A, 557, A26
Mashonkina, L. I., & Bikmaev, I. F. 1996, Astron. Rep., 40, 94
Mashonkina, L., & Belyaev, A. K. 2019, Astron. Lett., 45, 341
Mashonkina, L., Gehren, T., & Bikmaev, I. 1999, A&A, 343, 519
Mashonkina, L., Zhao, G., Gehren, T., et al. 2008, A&A, 478, 529
McCulloch, M. T., & Wasserburg, G. J. 1978, ApJ, 220, L15
Mott, A., Steffen, M., Caffau, E., Spada, F., & Strassmeier, K. G. 2017, A&A, 604, A44
Nordlander, T., Amarsi, A. M., Lind, K., et al. 2017, A&A, 597, A6
Nordlund, Å., & Galsgaard, K. 1995, A 3D MHD code for parallel computers, Tech. rep., Niels Bohr Institute, University of Copenhagen
Nordlund, Å., Galsgaard, K., & Stein, R. F. 1994, NATO Adv. Sci. Instit. Ser. C, 433, 471
Osorio, Y., Lind, K., Barklem, P. S., Allende Prieto, C., & Zatsarinny, O. 2019, A&A, 623, A103
Pavlenko, Y. V., Jenkins, J. S., Jones, H. R. A., Ivanyuk, O., & Pinfield, D. J. 2012, MNRAS, 422, 542
Rybicki, G. B., & Hummer, D. G. 1991, A&A, 245, 171
Rybicki, G. B., & Hummer, D. G. 1992, A&A, 262, 209
Seaton, M. J. 1962, in Atomic and Molecular Processes, ed. D. R. Bates (Cambridge, Massachusetts, USA: Academic Press), 375
Shchukina, N. G., Olshevsky, V. L., & Khomenko, E. V. 2009, A&A, 506, 1393
Short, C. I., & Hauschildt, P. H. 2006, ApJ, 641, 494
Silverans, R. E., Borghs, G., de Bisschop, P., & van Hove, M. 1986, Phys. Rev. A, 33, 2117
Smith, V. V., & Lambert, D. L. 1988, ApJ, 333, 219
Smitha, H. N., Nagendra, K. N., Stenflo, J. O., & Sampoorna, M. 2013, ApJ, 768, 163
Steffen, M., Prakapavičius, D., Caffau, E., et al. 2015, A&A, 583, A57
Stief, F., Löhner-Böttcher, J., Schmidt, W., Steinmetz, T., & Holzwarth, R. 2019, A&A, 622, A34
Strassmeier, K. G., Ilyin, I., & Steffen, M. 2018, A&A, 612, A44
Tandberg-Hanssen, E. 1964, ApJS, 9, 107
Thielemann, F.-K., Arcones, A., Käppeli, R., et al. 2011, Prog. Part. Nucl. Phys., 66, 346
Valenti, S., David, Sand, J., et al. 2017, ApJ, 848, L24
van Regemorter, H. 1962, ApJ, 136, 906
van Hove, L. 1982, in Evolution in the Universe (Geneva: CERN), 53
Villemoes, P., Arnesen, A., Heijkenskjold, F., & Wannstrom, A. 1993, J. Phys. B At. Mol. Phys., 26, 4289
Wendt, K., Ahmad, S. A., Buchinger, F., et al. 1984, Z. Phys., 318, 125

Appendix A: Information on the hyperfine structure

This following tables tabulate the complete hyperfine structure information of the four barium diagnostic lines we used.

Table A.1. HFS information on the barium 4554 Å line.

λ (Å)	Isotope	Relative strength
4553.9980	137	0.1562
4553.9985	137	0.1562
4553.9985	137	0.0626
4554.0010	135	0.1562
4554.0015	135	0.1562
4554.0020	135	0.0626
4554.0317	134	1.0000
4554.0317	136	1.0000
4554.0332	138	1.0000
4554.0474	135	0.4376
4554.0498	137	0.4376
4554.0503	135	0.1562
4554.0513	135	0.0311
4554.0537	137	0.1562
4554.0542	137	0.0311

Table A.2. HFS information on the barium 5853 Å line.

λ (Å)	Isotope	Relative strength
5853.6831	137	0.0875
5853.6851	135	0.0875
5853.6865	137	0.1001
5853.6865	137	0.0626
5853.6875	135	0.1001
5853.6875	135	0.0626
5853.6875	137	0.3499
5853.6875	137	0.0626
5853.6880	137	0.0248
5853.6880	138	1.0000
5853.6885	135	0.3499
5853.6890	136	1.0000
5853.6890	135	0.0248
5853.6890	135	0.0626
5853.6895	137	0.1249
5853.6899	135	0.1249
5853.6899	134	1.0000
5853.6904	137	0.1001
5853.6914	135	0.1001
5853.6934	135	0.0875
5853.6934	137	0.0875

Table A.3. HFS information on the barium 6141 Å line.

λ (Å)	Isotope	Relative strength
6141.7183	137	0.0041
6141.7202	137	0.0585
6141.7222	137	0.0064
6141.7231	135	0.0041
6141.7231	137	0.3750
6141.7231	137	0.0727
6141.7246	135	0.0585
6141.7251	137	0.2332
6141.7251	137	0.0562
6141.7266	137	0.1312
6141.7266	137	0.0626
6141.7261	135	0.0064
6141.7271	138	1.0000
6141.7271	135	0.3750
6141.7271	135	0.0727
6141.7280	136	1.0000
6141.7290	135	0.2332
6141.7290	135	0.0562
6141.7295	134	1.0000
6141.7300	135	0.1312
6141.7305	135	0.0626

Table A.4. HFS information on the barium 6496 Å line.

λ (Å)	Isotope	Relative strength
6496.8979	137	0.0311
6496.8989	135	0.0311
6496.9014	137	0.1562
6496.9019	135	0.1562
6496.9062	137	0.4376
6496.9067	135	0.4376
6496.9102	134	1.0000
6496.9102	136	1.0000
6496.9102	138	1.0000
6496.9160	135	0.0626
6496.9165	137	0.0626
6496.9175	135	0.1562
6496.9185	137	0.1562
6496.9204	135	0.1562
6496.9219	137	0.1562